Preparation of anisotropic magnetic $FeNiPt_2$ films on MgO(001): Atomistic mechanisms for the interdiffusion of two $L1_0$ phases

R. V. P. Montsouka, C. Goyhenex, G. Schmerber, C. Ulhaq-Bouillet, A. Derory, J. Faerber, J. Arabski, and V. Pierron-Bohnes*

IPCMS, CNRS UMR 7504-ULP, 23 rue du Læss BP43, 67034 Strasbourg Cedex2, France

(Received 24 January 2006; revised manuscript received 21 June 2006; published 16 October 2006)

$L1_0$-ordered $FeNiPt_2(001)$ thin films were prepared by the interdiffusion of FePt(001) and NiPt(001) layers codeposited on MgO(001) substrates by molecular beam epitaxy (MBE). A large uniaxial magnetic anisotropy (K_u=9.10^5 J/m^3) and a reduced magnetic transition temperature (T_c=400 K) were obtained. Growth at 700 K and a first annealing at 800 K result in a large long-range order parameter reflecting the concentration modulation along the growth direction. This high long-range order parameter is conserved in the $FeNiPt_2$ layers after interdiffusion at 900 K, contrary to what is expected from a simple vacancy migration process. This experimental observation can be explained either by a 6-jump cycle mechanism or by the alternate diffusion of a double vacancy, which are both favored energetically over a second-nearest-neighbor jump mechanism or the simultaneous diffusion of a double vacancy as shown by quenched molecular dynamics simulations.

DOI: 10.1103/PhysRevB.74.144409 PACS number(s): 75.70.−i, 66.30.Pa, 68.55.Jk, 66.30.Ny

I. INTRODUCTION

The super-paramagnetic behavior of nanometer magnetic dots, i.e., the thermal fluctuations of the magnetization due to the similar orders of magnitude of the magnetic and thermal energies, is today the limiting phenomenon in the storage density of magnetic media. A possible solution to drive back this superparamagnetic limit is to use a magnetic material with a large magnetic anisotropy K_u.

Chemically ordered FePt and CoPt thin films are very interesting due to both their magnetic anisotropy and magneto-optical response.[1–8] These films order in the $L1_0$ tetragonal structure (Fig. 1). This phase can be described starting from a face-centered-cubic (fcc) lattice. When the chemical order is complete, pure M (M=Co or Fe) planes and pure Pt planes alternate along the [001] direction of the initial fcc phase, which becomes the tetragonal axis of the $L1_0$ structure. This chemical order is accompanied by a slight tetragonal deformation of the lattice (c/a=0.93–0.96). When the $L1_0$ long-range order is incomplete, the long-range order parameter S quantifies the concentration difference between the Pt-rich (C_1) and the Pt-poor (C_2) planes: $S=C_1-C_2$ in a stoechiometric alloy (S=1 in completely ordered $L1_0$ structure and S=0 in the disordered fcc phase). The concentration modulation can occur along any of the 3 ⟨001⟩ directions of the fcc matrix. There are thus 3 variants of $L1_0$ grains depending on the concentration modulation direction: for instance, in the z variant, the concentration modulation is along the [001] direction. The high-T preparation of thin films on a single crystalline substrate with a (001) surface plane and an in-plane lattice parameter slightly larger than c favors the growth of the $L1_0$ z variant due to the conjunction of the Pt surface segregation, of the strains due to the substrate in the first atomic layers, and of the high mobility of atoms at the surface.[3,4]

The $L1_0$ structure leads in FePt and CoPt to a strong magnetic anisotropy along the tetragonal c axis as predicted by Daalderop, Kelly, and Schuurmans.[1] Many studies have been reported in FePt and CoPt alloy films obtained by conventional deposition techniques such as molecular beam epitaxy (MBE) and sputtering.[2–8] These alloy films exhibit a large magnetic anisotropy energy (K_u),[2,5] up to 10^7 J/m^3, and a large coercivity (H_c).[6–8]

As such, these alloys are interesting for perpendicular recording. Yet, their technological integration remains problematic. Indeed, such strong anisotropies involve a strong coercive field that is difficult to overcome with a miniaturized write head. A solution is to use ternary alloys by adding an element with a lower magnetic moment such as Ni that nevertheless conserves the $L1_0$ phase. Such intrinsic properties as the Curie temperature and the coercive field could then be adjusted so as to allow magnetic writing by a combination of laser heating and a reasonable perpendicular magnetic field.

The intrinsic perpendicular magnetic anisotropy energy K_u for $(Fe\text{-}Co\text{-}Ni)_{50}Pt_{50}$ quaternary alloy thin films as a function of structure and composition was discussed by Kanazawa and Suzuki.[9] These authors estimated the K_u values extrapolated to S=1 for different Fe concentrations beyond 50 at. % in $(Fe\text{-}Co)_{50}Pt_{50}$ and $(Fe\text{-}Ni)_{50}Pt_{50}$ alloy thin films. They found in both systems that K_u decreases with the total number of valence electrons.

Several structural and magnetic studies on FePt, NiPt, and $Fe_xNi_{1-x}Pt$ bulk alloys were reported.[10–13] The order-disorder transition temperature is respectively 903 K, 1570 K, and

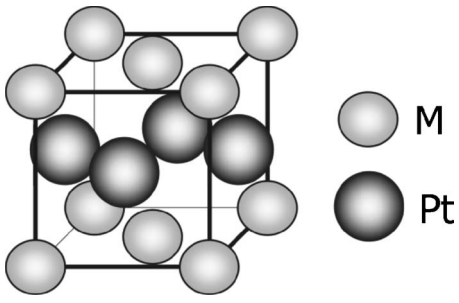

FIG. 1. $L1_0$ ordered phase.

TABLE I. Thin film preparation, annealing parameters and physical properties for the different samples: the growth temperature T_S, the temperature (T_A) and duration (t_A) of annealing, the "epitaxy quality" Q_E, the lattice parameters c, a and their ratio c/a, the long-range order parameter in the z variant S, the rocking curve width of the 002 peak $\Delta\omega$, the magnetic anisotropy energy K_u, the coercive field in perpendicular $H_{C\perp}$ the saturation magnetization M_S, and the relative remanent magnetization M_R/M_S. Except for T_A, the number in parentheses gives the error bar on the last digit. Samples with "b" in their names integrate a 10 nm Pt buffer.

Sample name	Alloy	T_S (K)	T_A (K) [t_A(h)]	Q_E	c (nm)	a (nm)	c/a	S	$\Delta\omega$ (°)	K_u (MJ/m^3)	$H_{C\perp}$ (mT)	M_S (kA/m)	M_R/M_S
N1b	NiPt	650		0.63(2)	0.364(5)	0.378(6)	0.963	0.56(7)	1.74(3)				
N2b	NiPt	700		0.74(2)	0.361(4)	0.380(6)	0.950	0.69(6)	1.78(5)				
N3b	NiPt	750		0.93(2)	0.362(4)	0.382(6)	0.948	0.40(5)	1.57(8)				
N4b	NiPt	800		0.72(2)	0.359(2)	0.385(3)	0.932	0.89(5)	1.16(1)				
F1b	FePt	700		0.50(2)	0.372(3)	0.389(6)	0.956	0.64(6)	1.45(7)	5.2(3)	639	1036	0.73
F2b	FePt	800		0.22(2)	0.373(3)	0.389(7)	0.959	0.61(7)	1.47(4)	—	601	—	—
F3b	FePt	850		0.53(2)	0.374(4)	0.385(7)	0.971	0.58(8)	1.51(8)	—	—	—	—
N5	NiPt	700	700(24)	0.78(2)	0.368(5)	0.373(6)	0.987	0.29(10)	1.92(3)				
F4	FePt	700	700(24)	0.77(2)	0.369(4)	0.395(7)	0.934	0.69(5)	1.83(3)	7.2(4)	310	1237	0.977
F5	FePt	750	750(12)	0.68(2)	0.372(3)	0.388(5)	0.959	0.70(5)	1.68(2)	7.6(4)	333	1016	0.98
F6	FePt	800	750(12)	1.00	0.373(3)	0.388(6)	0.961	0.60(7)	1.63(3)	7.4(4)	396	947	0.96
F7	FePt	850	750(12)	0.85(2)	0.372(2)	0.389(6)	0.956	0.72(5)	1.88(3)	7.3(4)	384	1061	0.94

1323 K in NiPt, FePt, and $FeNiPt_2$. Moreover, the Curie temperature of the $Fe_{1-x}Ni_xPt$ ternary alloys decreases with increasing the nickel content.[11]

In this paper, we show that $FeNiPt_2$ films with a single variant and a high $L1_0$ chemical order ($S \approx 0.7$) can be obtained by annealing FePt/NiPt bilayers at 900 K. Another interesting result of our work is that the interdiffusion between NiPt and FePt occurs without destroying the $L1_0$ long-range order. Quenched molecular dynamic simulations show that the 6-jump cycle or a bivacancy alternate jump mechanisms are energetically favorable compared to a second-nearest-neighbor (2^{nd}-nn) jump or a bivacancy simultaneous jump mechanism. Either of these favorable mechanisms would explain our experimental observations.

In the next section of the paper, we describe the sample preparation and experimental details. Section III is focused on the structural study, while the magnetic study is described in Sec. IV. We discuss our results and present our simulations in the last section.

II. PREPARATION AND EXPERIMENTAL DETAILS

The ternary alloy layers were prepared in three steps. First, we deposited a 25 nm-thick $L1_0$ FePt(001) layer by MBE on a MgO(001) substrate. Second, a 25 nm-thick $L1_0$ NiPt(001) layer was grown over it by the MBE. Finally, we annealed these bilayers to produce the tetragonal $FeNiPt_2$ intermetallic phase with the crystallographic c-axis oriented perpendicularly to the film plane.

In a preliminary study, we optimized the growth conditions of the binary anisotropic FePt and NiPt alloy thin films by MBE codeposition on MgO(001). Several FePt and NiPt films were coevaporated by the MBE in ultrahigh vacuum (base pressure lower than 10^{-9} mbar and pressure during evaporation around 10^{-8} mbar) on MgO(001) substrates, with or without a Pt buffer layer. The FePt and NiPt samples are named Fp and Np, respectively (Table I), with p their chronological rank. A label "b" is added for the samples with a 10 nm Pt buffer. Several deposition temperatures (T_S) were used in order to optimize the growth quality and the long-range ordering. The results are given in Table I. Examples of RHEED patterns recorded during the growth are shown in Fig. 2.

The precise measure of the film thickness is important to be able to compare the x-ray diffraction intensities and the magnetic properties between different samples and to estimate the composition of the ternary alloy. The film thickness was deduced from x-ray reflectometry spectra. We used a Philips reflectometer operating with Cu $K\alpha$ radiation. The spectra were adjusted with the program developed by Fischer[14] to extract the thickness of the different layers and the roughness of the interfaces.

These thickness of the alloys and their composition were confirmed using a scanning electron microscope (x-ray energy dispersive spectrometry). Spectra at three primary energies (4, 8, and 12 keV) were acquired. The normalized emission intensity of each element present in the layer or the substrate was computed thanks to the Stratagem matrix correction software for layered samples (from SamX), using a correction method based on a realistic distribution of in-depth ionization and thin film standards.

Two $FeNiPt_2$ ternary alloy thin films (named FNp) were fabricated by annealing some NiPt/FePt binary alloy bilayers deposited at 700 K directly on MgO(001) substrates (Table II). The bilayers were annealed *ex situ* (under 10^{-6} mbar vacuum), first at 800 K for up to 2.5 h and then at 900 K for up to 12 h.

After sample growth and annealing, it was important to obtain information on the structure of the samples: what proportion of grains is epitaxial? What is the quality of the crystallographic order? What is the $L1_0$ long-range order param-

TABLE II. Same as Table I for bilayers.

Sample name	Alloy	T_S (K)	T_A (K) $[t_A(h)]$	Q_E	c (nm)	a (nm)	c/a	S	$\Delta\omega$ (°)	K_u (MJ/m^3)	$H_{C\perp}$ (mT)	M_S (kA/m)	M_R/M_S
FN1	FePt	700		0.45(5)	0.369(4)	0.396(7)	0.932	0.32(11)	1.71(4)	5.1(3)	320	1167	0.89
	NiPt	700		0.41(5)	0.367(4)	0.376(6)	0.976	0.37(10)	1.66(4)				
FN1	FePt		800(2.5)	0.48(5)	0.368(5)	0.390(6)	0.944	0.67(5)	1.64(4)	7.5(4)	312	1200	0.93
	NiPt		800(2.5)	0.55(5)	0.359(2)	0.380(4)	0.945	0.74(4)	1.40(4)				
FN1	$FeNiPt_2$		800(2.5) +900(12)	0.72(4)	0.363(2)	0.389(4)	0.933	0.71(4)	0.92(6)	0.90(3)	64	517	0.05
FN2	FePt	700		0.45(5)	0.369(4)	0.395(7)	0.934	0.50(7)	1.89(4)	7.0(4)	357	1018	0.93
	NiPt	700		0.51(5)	0.359(2)	0.384(4)	0.935	0.42(8)	1.51(5)				
FN2	FePt		800(2.5)	0.48(5)	0.368(4)	0.395(7)	0.932	0.72(5)	1.63(4)	7.8(4)	320	1045	0.98
	NiPt		800(2.5)	0.69(5)	0.358(3)	0.385(5)	0.930	0.88(4)	1.26(2)				
FN2	$FeNiPt_2$		800(2.5) +900(12)	0.77(4)	0.363(2)	0.387(3)	0.938	0.67(7)	0.90(7)	0.91(3)	68	520	0.05

eter? This structural information on the samples was obtained by x-ray diffraction (XRD) on a Brüker D500 diffractometer (Co-K_α $\lambda=0.1789$ nm) and completed by transmission electron microscopy observations. A home-made XRD sample holder allowed the optimization of the sample position so as to maximize the 002 peak[15] intensity of the $L1_0$ phase $\theta/2\theta$ and rocking curves were systematically measured. We thus deduced the "epitaxial quality" (Q_E) and the

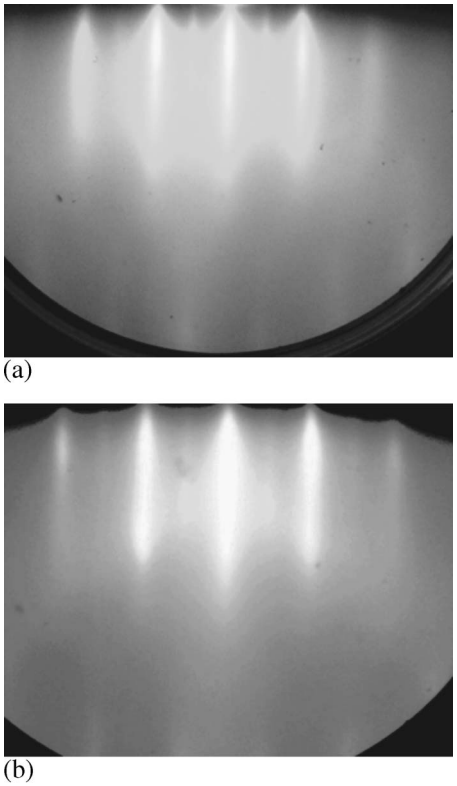

(a)

(b)

FIG. 2. (a) RHEED pattern after depositing the FePt layer (sample FN2), (b) RHEED pattern after depositing the NiPt layer (sample FN2). The RHEED beam is directed along the ⟨100⟩ MgO azimuth.

$L1_0$ long-range order (S) of the z variant of the $L1_0$ phase as follows:

—As the [001] growth direction (tetragonal axis) is the interesting growth orientation for high perpendicular anisotropy, we define the "epitaxial quality", Q_E, as the volume fraction of the [001]-oriented grains. We chose to determine it through $Q_E=E\,I_{002}/I_{\max}$ where I_{002} is the integrated intensity of the $L1_0$-phase 002 peak and $I_{\max}$ is the integrated intensity of this peak in sample F6. As a matter of fact, transmission electron microscopy diffraction (selected area diffraction performed on a plane-view sample observable on an area larger than 1 mm^2) showed that F6 is fully [001] oriented. E is a normalization factor taking into account the thickness, the diffusion factor at the 002 peak, and the atomic density of the films. With this definition, Q_E equals 1 for a fully [001]-oriented sample.

—The $L1_0$ long-range order of the z variant, S, can be obtained by comparing the intensity of a superstructure peak of the z variant (hkl with the parity of l different from that of h and k) with that of a fundamental peak of the same variant[16] (hkl with the same parity). We used the intensity ratio between 001 and 002 peaks after corrections for polarization, illumination, and absorption using the method developed by Cohen *et al.*[17]

To check if the other 2 variants are present (i.e., those with in-plane concentration modulations), we searched for their superstructure peak (hkl with the parity of h different from that of k and l for the x variant, hkl with the parity of k different from that of h and l for the y variant). The difficulty is that these peaks can only be measured in asymmetrical geometry. Thus the sample has to first be oriented within its plane so as to make the scattering plane coincide with the reciprocal space plane containing one of these peaks. The 203 (resp. 023) peak was thus optimized before the 102 (resp. 012) peak could be searched for, using rocking curve measurement to account for the shift due to tetragonalization.

As these films are mainly interesting for their magnetic properties, we also performed classical magnetic measurements. Magnetization cycles were obtained at 4 K and room temperature using a SQUID magnetometer (maximum field

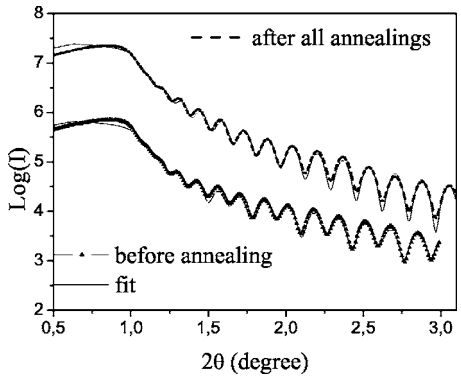

FIG. 3. Reflectivity curves on the FN1 sample: as-prepared and after annealing (2 h 30 at 800 K and 12 h at 900 K).

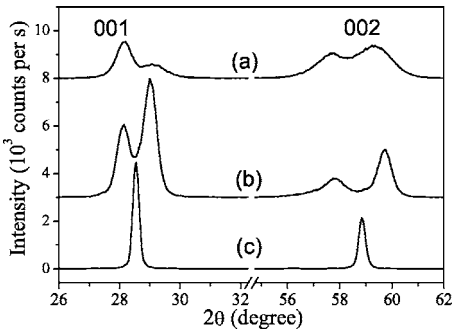

FIG. 4. XRD $\theta/2\theta$ spectra of the FN1 25 nm NiPt/25 nm FePt/MgO(001) bilayer (a) as deposited, (b) after annealing at 800 K during 2 h 30, and (c) after further annealing at 900 K during 12 h. The intensity of curve (c) was divided by 10.

5 T). Furthermore, the magnetic domains were imaged by magnetic force microscopy (MFM) using a Nanoscope III from Digital Instruments in vibrating mode with a commercial magnetic tip (a pyramidal Si tip covered with sputtered CoCr). The lateral resolution was about 50 nm. Before the MFM measurements, the samples were demagnetized by cycling an external magnetic field applied perpendicular to the film plane (with amplitude decreasing from 1.3 T down to 0 T in 0.01 T steps).

III. STRUCTURAL RESULTS

The epitaxial growth of the FePt and NiPt layers was first qualitatively confirmed by RHEED (Fig. 2). The observed streak pattern shows that their surface is flat on an atomic scale. The thinner streaks in FePt are an indication of superior flatness than in NiPt/FePt.

The XRD results reported in Tables I and II show that:

(1) NiPt and FePt films deposited without a Pt buffer layer have a high Q_E ($Q_E > 0.65$).

(2) NiPt grows with a better quality than FePt on the Pt buffer layer.

These observations led us to grow the FePt layer before the NiPt layer, when synthesizing the bilayers.

(3) During the 800 K annealing of FN1 and FN2, Q_E increases and the 002 peak width decreases, indicating a size increase of the [001]-oriented grains.

Regarding the FePt films deposited on a Pt buffer, grains with a nonepitaxial growth ([111] textured) are observed for both Pt and FePt. Moreover, for a substrate temperature T_S larger than 800 K, interdiffusion takes place at the interface between the Pt buffer layer and the FePt layer. On the contrary, the FePt films deposited without Pt buffer layer are [001] single crystals with no [111] grains. For all these reasons, we have chosen the deposition of the FePt film directly on the substrate and before the NiPt film, when preparing the bilayers.

The curves of x-ray reflectivity obtained on FN1 and FN2 after deposition exhibit a beating every two minima that is characteristic of two layers with equal thickness (lowest curve in Fig. 3). After the second annealing, the beating disappears, indicating a complete interdiffusion and the formation of a homogeneous layer.

The curve adjustment allowed us to estimate the thickness of the layers and the roughness of each surface and interface. We obtained for instance a thickness of (24.8±1.0) nm for FePt and (25.0±1.0) nm for NiPt in FN1 and FN2 samples. The thickness at the end of annealing is 51.7±1.0 nm for sample FN1 and 51.0±1.0 nm for sample FN2. The curves are not damped at large angles, confirming the flatness of the samples observed by RHEED. A roughness smaller than 0.1 nm was found at all interfaces for all samples.

Figure 4 shows the x-ray diffraction spectra of FN2 (a) before annealing, (b) after a first 2h30 annealing at 800 K and (c) after a second annealing at 900 K for 12 h. After the annealing at 800 K, no interdiffusion is observed. Q_E increases mainly in the NiPt layer (0.5 to 0.7). The $L1_0$ order is increased in both layers: the 001 (and 003, not shown here) peaks are more intense for both NiPt (peak on the right) and FePt (peak on the left). For example, the long-range order parameter S increases from 0.42 to 0.88 for the NiPt layer in the FN2 sample. Moreover, the rocking curves are narrower, indicating an enhancement of the order coherence length within the grains. These changes are responsible for the 001 peak intensity inversion in Fig. 4(b) compared to Fig. 4(a). After the 800 K annealing, the lattice parameters also become closer to the values given in Ref. 19 ($a=0.3823$ nm and $c=0.3589$ nm for NiPt and $a=0.3838$ nm and $c=0.3715$ nm for FePt) for bulk materials prepared with the maximum possible $L1_0$ order.

Interdiffusion is complete after the 12 h annealing at 900 K. The x-ray diffraction in Fig. 4(c) does not present any 002 peak for the x or y variants; this peak would appear at a slightly smaller θ value than the 002 peak of the z variant. Moreover, in both FN1 and FN2, the 102 (resp. 012) asymmetrical peak could not be found in the sample orientation while the 203 (resp. 023) peak was clearly visible. This indicates that the $L1_0$ phase has maintained its z variant property, i.e., that the initial ordered phase was conserved during interdiffusion, because if it had been destroyed during interdiffusion and formed again in a second step, all 3 variants should be present in equivalent proportions.

The rocking curves of the 001 and 002 peaks are very narrow (width smaller than 0.7° and 0.9°, respectively). The composition analysis by scanning electron microscopy gave (27%±2%) Fe (28%±2%) Ni (45%±4%) Pt in FN1 and

(26% ±2%) Fe (27% ±2%) Ni (47% ±4%) Pt in FN2.

IV. MAGNETIC PROPERTIES

Magnetization cycles were collected at 300 K with the magnetic field applied both in the parallel and perpendicular directions to the film plane. To obtain the magnetic anisotropy, K_{eff} the area between both curves was calculated. The uniaxial anisotropy energy (K_u) is obtained by correcting K_{eff} from the contribution of the magnetostatic energy $2\pi M_S^2$.

Because of the small relative volume of the ferromagnetic alloy, the data were corrected for the MgO diamagnetic contribution. The magnetic cycles were measured at 300 K in order to avoid paramagnetic contributions due to substrate impurities. As the susceptibility varies from one MgO substrate to another (owing to different impurity concentrations), the MgO contribution to the magnetization was evaluated in each sample in the easy direction. Indeed, above the saturation of the ferromagnetic contribution of the layer, the slope of the magnetization is only due to the diamagnetic contribution of the substrate. It was assumed to be identical in the other directions.

Figure 5 presents the magnetic hysteresis loops in and out of plane, both before and after the 900 K annealing. In both cases, the easy magnetization axis is perpendicular to the film plane. Both samples have a large perpendicular magnetocrystalline anisotropy. Before interdiffusion, because the ordered NiPt layer is not magnetic,[10] the magnetic properties are those of the FePt layer and the in-plane magnetization does not saturate up to 5 T.

After interdiffusion, the saturation field is 3.5 T. Moreover, we obtained a 6.8 mT coercive field that is smaller than the coercive field measured in the 50-nm FePt thin films (350 mT). The saturation magnetization is 0.52 MA/m. This uniaxial anisotropy energy (0.9 MJ/m^3) is smaller than the uniaxial anisotropy energy of CoPt ordered thin films[4] (4 MJ/m^3) and is comparable to the uniaxial anisotropy energy of FePd ordered thin films[21] (1.2 MJ/m^3).

The magnetization was also measured as a function of temperature at 0.11 T, yielding a Curie temperature $T_C \sim 400$ K [inset in Fig. 5(b)] for both samples, as expected from T_C in the bulk alloys.[10] At 4 K, the magnetization of the ternary alloy is 0.64 MA/m.

MFM images were obtained on the demagnetized $L1_0$ single-crystalline samples with the magnetic field directed along the easy magnetization axis. For all samples, MFM images display highly interconnected stripes corresponding to up and down orientations of the magnetization, similar to those observed in [001]-oriented $L1_0$ FePd or CoPt thin films.[20,21,4] Figure 6 presents the MFM images of FN2 sample before and after annealing. Each annealing increases the magnetic contrast. After the 900 K annealing [Fig. 6(c)], the domain-wall width is the lowest and the magnetic contrast the strongest. The experimental average size of the domains, d_{meas}, obtained using the Fourier transform of the images, was 190 nm for FePt and 210 nm for $FeNiPt_2$.

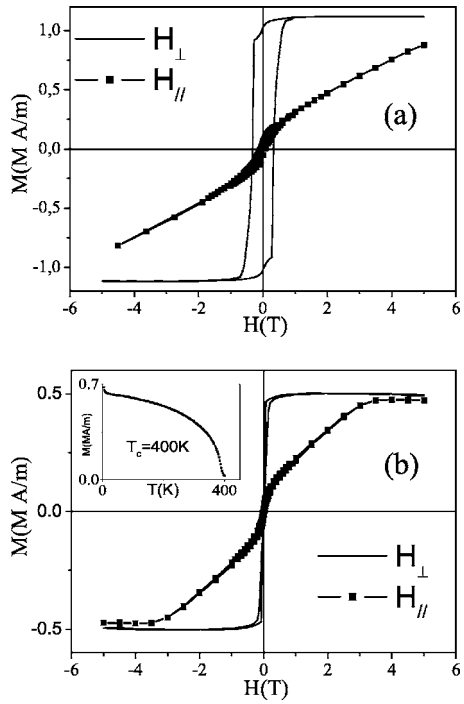

FIG. 5. Magnetization hysteresis loops on FN2 (a) before annealing [25 nm NiPt/25 nm FePt/MgO(001)] and (b) after interdiffusion at 900 K during 12 h [we obtain 50 nm $NiFePt_2$/MgO(001)]. The curves are recorded by SQUID at room temperature with the external magnetic field perpendicular (easy magnetization axis) or parallel to the film plane (hard magnetization axis). The inset shows the temperature dependence of the magnetization for $H=0.11$ T after interdiffusion.

V. DISCUSSION

A. Structural results

The RHEED images and the reflectivity curves yield results regarding the roughness of the surface and of the interfaces that are in good agreement for all samples. Both techniques indicate that the films are flat. This point is important because the flatness of the surface during the growth favors the growth of the z variant with a large lateral coherence within the growth plane. As a matter of fact, it has been shown that in these $L1_0$ phases the growth along the [001] direction is a two-layer by two-layer growth,[22] due to a tendency for Pt surface segregation.[23] A large roughness would lead to many antiphase boundaries and would strongly decrease the 001 peak intensity due to destructive interferences.

The crystalline quality Q_E and the long-range order parameter increase considerably in the NiPt layer during the first annealing. It is remarkable that the z variant grains become larger and more ordered without any nucleation of the other two variants. This can be attributed to the strains due to epitaxy present in these grains. As a matter of fact, these strains are tensile in the film plane and compressive out of plane, in concordance with the tetragonalization in the z variant. In the FePt layer, the ordering is more limited during the first annealing because the FePt layer was annealed at 700 K during the 50 min of the NiPt deposition.

The difference in Pt composition, which is higher in the FN1 than in the FN2 sample, explains the small difference in

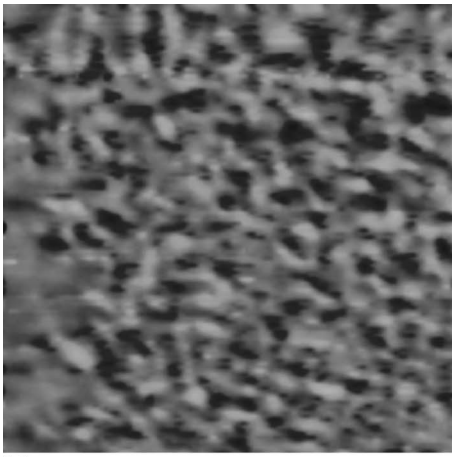

(a)

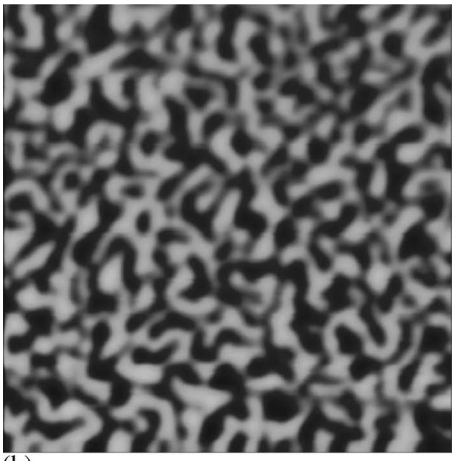

(b)

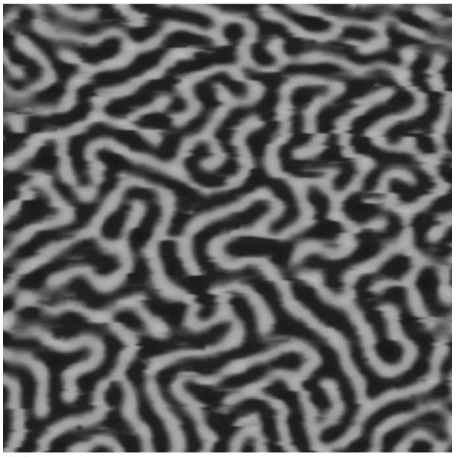

(c)

FIG. 6. MFM images on FN2 (size of the image: 5×5 μm^2). The images were obtained for a perpendicularly demagnetized state (a) before annealing, (b) after annealing at 800 K during 2 h 30, and (c) after further annealing at 900 K during 12 h.

lattice constant between FN1 and FN2. Moreover, the lattice parameters of NiPt ($c=0.359$ nm and $a=0.382$ nm) are lower than those of FePt ($c=0.372$ nm and $a=0.386$ nm), explaining the systematic small difference in Ni *versus* Fe composition in the ternary alloys prepared from FePt and NiPt layers with the same thickness.

B. Magnetic results

In Fig. 5(b), the magnetization hysteresis loops recorded with the magnetic field parallel to the film plane exhibits a small contribution of grains with an in-plane easy-magnetization axis. Its relative amplitude (0.25) is in agreement with Q_E measured in the annealed sample (0.77) because the grains with a [111] growth direction are either disordered or ordered with an easy-magnetization axis that is not perpendicular to the film.

The substitution of Fe atoms with Ni atoms causes a decrease in the saturation magnetization and consequently in both the coercivity and the anisotropy magnetic energy. This result was also obtained by Li *et al.*[24]

Kooy and Enz[25] have developed a model in equivalent systems to relate the domain width to the magnetic anisotropy, the magnetization and the exchange energy. In FePt where all magnetic data are known ($A\approx10^{-11}$ J/m;[26] $M_S\approx1.061\times10^6$ A/m; $K_U\approx7.3$ MJ/m^3), we can compare the measured and calculated domain sizes. Using this formula, we obtain $d(\mathrm{FePt})=173$ nm, in good agreement with the measured value (190 nm). In $FeNiPt_2$ we did not find any estimation for A and the comparison could not be made.

C. Evolution of the concentration profile during heat treatments

Rennhofer *et al.*[27] have studied the interdiffusion of multilayers consisting in a stacking of ^{57}FePt (2 nm) and FePt (3 nm) layers in the z variant of the $L1_0$ phase that are epitaxied on MgO(001) by MBE. Using the diffusion coefficients measured in the same temperature range, we have simulated the interdiffusion expected in the 25 nm NiPt/25 nm FePt bilayers assuming that the diffusion coefficients are identical in FePt and in $Ni_xFe_{1-x}Pt$ at any concentration. The Fe fraction x in the Fe_xNi_{1-x} planes is calculated using Fick's laws. We thus obtain the profiles shown in the insets to the panels of Fig. 7.

The main parts of Fig. 7 display the simulations of the specular XRD spectra for these concentration profiles. The Pt fraction in the Pt-rich planes is assumed to be always equal to 1. The intensity was calculated using the classical formula

$$I=A(\theta)A^*(\theta) \text{ with } A(\theta)=\sum_{j=1}^{N}\left\{F(j)e^{iQd(j)}\prod_{k>j}e^{-2\mu(k)d(k)/\sin\theta}\right\}.$$

N is the number of atomic layers, Q the wave vector, $\mu(k)$ the absorption coefficient of layer k, $d(j)$ the distance between the Pt and Fe_xNi_{1-x} planes, and $F(j)$ the atomic scattering factor of the species in plane j.[18] The FePt and NiPt contributions are clearly distinguished as long as the pure binary phases are present.

The experimental x-ray diffraction curves show the separation of the NiPt and FePt peaks after deposition as predicted by the simulations. This separation allowed us to monitor interdiffusion using x-ray diffraction and to observe (Fig. 4) that no interdiffusion was visible after the 2 h 30 annealing at 800 K, whereas interdiffusion was almost complete after the 12 h annealing at 900 K [with a final concentration spread smaller than 0.1 as deduced from the 002 peak

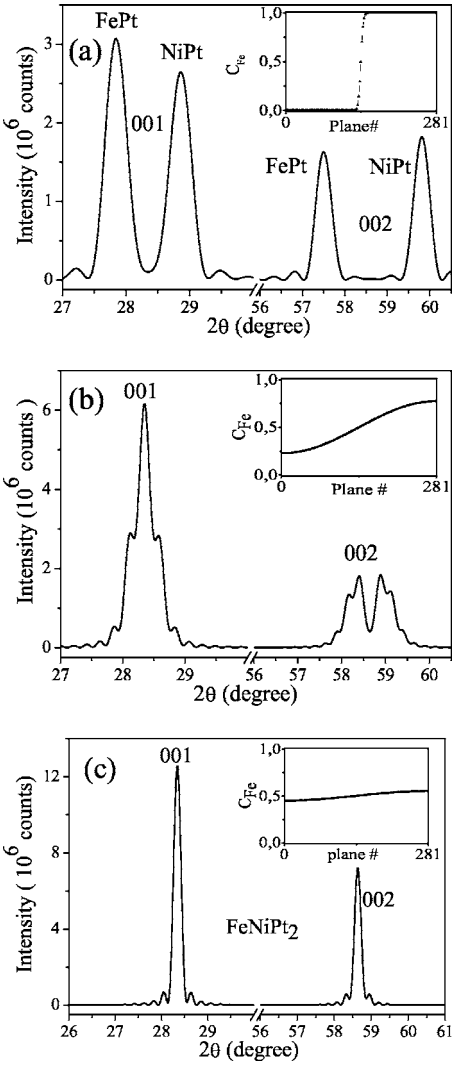

FIG. 7. Simulated spectrum of specular XRD in 25 nm NiPt/25 nm FePt with the concentration profiles shown in the inset: (a) after a 2 h 30 anneal at 800 K ($D=25\times10^{-24}$ m s^{-2} from Ref. 27), (b) after an additional 12 h anneal at 900 K ($D=312\times10^{-24}$ m s^{-2} is one standard deviation above the value found in Ref. 27), and (c) after an additional 12 h annealing with $D=5000\times10^{-24}$ m s^{-2}.

width in Fig. 4(c) and simulated in Fig. 7(c)].

Experimentally, we indeed observe a dramatic difference in interdiffusion between both annealing conditions. The interdiffusion is very limited during the 2 h 30 anneal at 800 K [Fig. 7(b)] and much more effective during the 12 h anneal at 900 K [Fig. 7(c)]. Nevertheless we find that the interdiffusion is not complete after a 12-h annealing at 900 K in the simulation with the data from Ref. 27, contrary to the experimental diffraction results. The diffusion is thus higher in the FePt/NiPt bilayers than in the FePt multilayers of Rennhofer *et al.*[27]

Several explanations can be invoked: (i) the diffusion coefficient may be higher in $Ni_xFe_{1-x}Pt$ than in FePt and depends on the nickel concentration, (ii) a driving force due to the departure of the thermodynamical activity from that of an ideal solution (i.e., the system is too far from equilibrium)

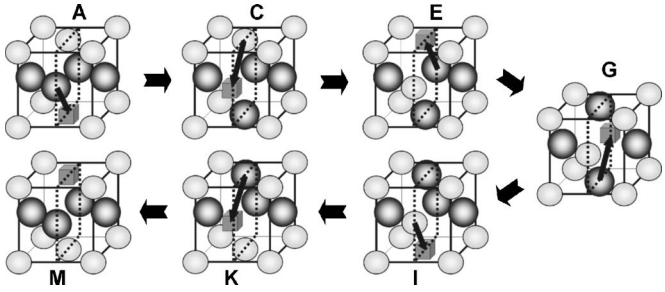

FIG. 8. 6-jump cycle in a CoPt $L1_0$ structure (Co is the small atom). The global result of the cycle is the exchange of a Co atom and a 2nd-nn Co-vacancy through the Pt plane. This cycle allows the migration of Co atoms along the z direction without destroying the $L1_0$ long-range order.

may be present in the FePt/NiPt bilayer near the interface, whereas in the FePt/^{57}FePt the process is truly a random walk, (iii) our samples present a nonnegligible proportion of nonepitaxial grains [$(1-Q_E)$ in Table I], which implies the presence of grain boundaries. The diffusion is known to be much more efficient at grain boundaries than inside the grains. Moreover, grain boundaries also play the role of a vacancy reservoir. The presence of grain boundaries can thus change appreciably the diffusion properties. Rennhofer *et al.* do not present any evaluation of the nonepitaxial grain proportion in their samples. Their proportion may be smaller than ours since the FePt layers can be grown at higher temperature than NiPt layers. Moreover, the typical diffusion length in their case is 2.5 nm (half width of the bilayer) whereas in our case it is 20 times larger. They are thus less sensitive to grain boundary effects. Hence, all these reasons explain the difference between the calculated and the observed spectra after the 12 h annealing at 900 K.

D. Effects of annealing on $L1_0$ long-range order

The x-ray diffraction curves after the different thermal treatments also show that ordering takes place without interdiffusion in a first step, whereas interdiffusion takes place without destroying the preferential [001] order in a second step. The same phenomenon has been observed by Rennhofer *et al.*[27] when interdiffusing the $(^{57}FePt/FePt)_N$ multilayers: the interdiffusion of both Fe isotopes in a well ordered single z variant $L1_0$ phase occurred with no decrease in the long-range order. This is very interesting because interdiffusion along the z direction through the direct migration of single vacancies thanks to nearest-neighbor jumps would destroy the existing z variant order as a vacancy leaves a string of antisites behind it (see the first 2 steps in Fig. 8). This suggests that interdiffusion occurs through another mechanism that maintains the $L1_0$ order. The 2nd-nn jumps are the natural jumps for such diffusion without order change, but their occurrence probability is very small due to the large elastic energy (3.9 eV, see Fig. 9) at the saddle point position. In the $B2$ phase, where the vacancies also form an antisite at each step, the 6-jump cycle (6JC) mechanism has been proposed.[28,29] The vacancy makes a cycle of 6 jumps between 3 planes, following twice the same trajectory to re-

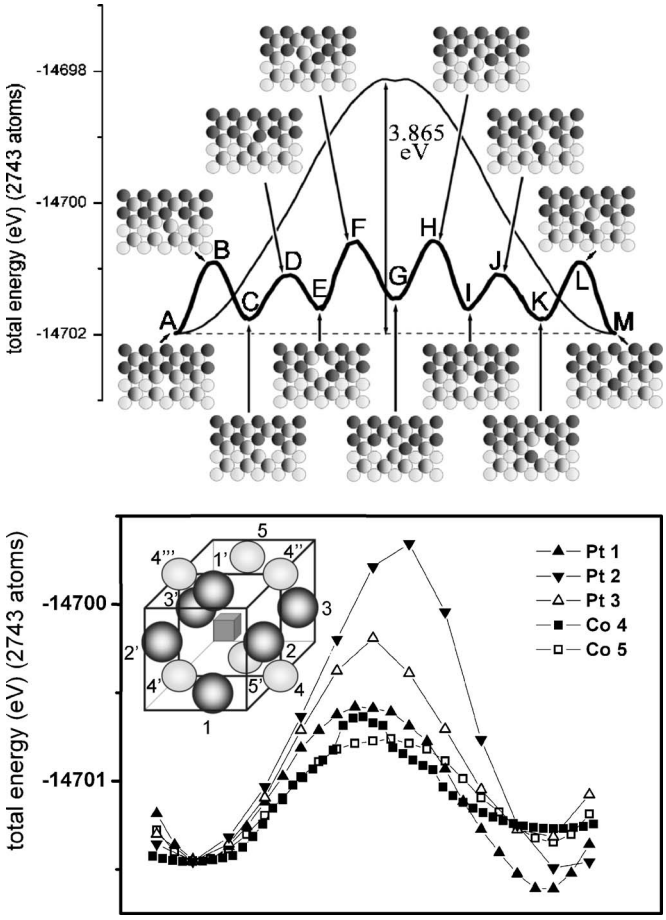

FIG. 9. (a) Total energy variation for a direct 2nd-nn jump (thin line) and for the 6 jump cycle (thick line). Configurations of the (100) plane containing the vacancy calculated by quenched molecular dynamics at several stages. The different energy levels are compared to $E_A=E_M$: $E_B=E_L=1.08$ eV; $E_C=E_K=0.21$ eV; $E_D=E_J=0.89$ eV; $E_E=E_I=0.37$ eV; $E_F=E_H=1.40$ eV; $E_G=0.53$ eV. (b) Total energy variation for every 1st-nn jump possible starting from G. The barrier energies are 0.87, 0.82, and 0.69 eV for Pt1; Co4, and Co5, respectively whereas the energy balance (difference between initial and final energies) are −0.16, +0.11 and +0.18 eV. The names of the different atoms are shown in insert. P, P′, etc. are equivalent due to the symmetry of configuration G with regard to the horizontal plane containing the vacancy and the vertical plane containing the vacancy and the antisites. For clarity, we only show the atoms 1st-nn of the vacancy.

cover the long-range order during the second crossing (last 3 steps in Fig. 8). Two driving forces can be at the origin of this mechanism. The ordering energy is opposed to the formation of many antisites. Epitaxial strain (tensile in the film plane and compressive out of plane) impedes the nucleation of another phase (either the disordered phase or another variant of the $L1_0$ phase) within a z variant grain.

Moreover, due to the proximity of the surface, the probability of a double vacancy occurring is not negligible. An interdiffusion mechanism, whereby an M-Pt-double vacancy propagates perpendicularly to the concentration modulation of the $L1_0$ structure, can thus be effective.

To get an insight into the energy cost of these mechanisms in FePt/NiPt and $(^{57}\mathrm{FePt/FePt})_N$ multilayers, we made some quenched molecular dynamics (QMD) calculations based on the second moment approximation of the tight-binding (TB) formalism. We performed these calculations in the CoPt system for which the parameters of the interaction potential are well known,[30] as opposed to FePt and NiPt systems, let alone the ternary $Ni_xFe_{1-x}Pt$ alloy. Co, Fe, and Ni have very similar cohesion energies and phase diagrams (they all contain the $L1_0$ structure with a critical temperature between 920 and 1570 K); we have therefore considered that the calculation in the case of CoPt will give a good first insight into the physics of the phenomenon.

E. Tight-binding quenched-molecular-dynamics (TB-QMD) in CoPt

The principles of the TB-QMD method are described in detail in Refs. 30–32. QMD is a relaxation procedure that evaluates the equilibrium positions at $T=0$ K of a finite number of atoms, by integrating the classical equation of motion. This numerical technique requires the use of realistic N-body potentials from which the energy E_i of an atom at a site i is derived. For transition metals the tight-binding formalism, within the second moment approximation, provides the following expression of the energy E_i of an atom i:

$$E_i = A\sum_j e^{-p(r_{ij}/r_0-1)} - \sqrt{\xi^2\sum_j e^{-2q(r_{ij}/r_0-1)}}, \qquad (1)$$

where r_0 is either the nearest neighbor distance in the metal Co (or Pt) for pure Co-Co (or Pt-Pt) interactions or $r_0=[r_0(\mathrm{Co})+r_0(\mathrm{Pt})]/2$ for mixed interactions. The summations run on the j atoms located in the 1st- and 2nd-nn shells of atom i.

The parameters A, p, q, and ξ are obtained by fitting experimental structural and cohesive properties of the pure materials and corresponding alloys. The parameters for the CoPt system are taken from Ref. 30. For the application to CoPt $L1_0$ alloy, we have used a slab of 14 (100) planes containing 14×14 atoms, with periodic conditions in x, y, and z directions, and alternate Co and Pt occupation of planes along the z direction. The lattice parameters were optimized to minimize the total energy. We found: $a=0.390$ nm and $c=0.3515$ nm so that $a/c=1.1$. Considering that the simulation corresponds to perfect order whereas the experimental value ($a/c=1.04$) does not, the tetragonality of the alloy is reasonably reproduced thanks to our semiempirical potential. A vacancy was created in the middle of the slab on the Co lattice. For each jump of the vacancy, one chosen atom was moved successively in small steps toward the vacancy. The system was then relaxed with two constraints:

(1) The bottom plane of the slab was fixed to avoid a global motion of the crystal,

(2) The jumping atom could move only perpendicularly to its trajectory.

The ability to relax the atomic positions around the vacancy is here a crucial step because calculations on a rigid lattice lead to an overestimation of the barriers. The total energy of the system can thus be plotted as a function of the fictive progress of the vacancy deduced from the progress of the different jumping atoms.

The most favorable processes of successive jumps were selected among various possibilities where atoms (Co or Pt) are found, after the jump, in various environments either in antisite positions or not. In this way, the initial jump of a nn Pt atom in the vacancy has a barrier of 1.08 eV, smaller than that of 1.30 eV for the jump of a nn Co atom in the same z plane. Therefore our sequence of favorable jumps starts with the jump of a Pt atom in the initial vacancy. Figure 9 shows the variation of the total energy for the 6JC together with the curve obtained for a 2^{nd}-nn jump that may also occur. At different stages, we show the atom positions in the (100) plane (dotted plane on Fig. 8) around the vacancy in the relaxed state as obtained by TB-QMD. The maximum energy attained during the 6JC (1.4 eV) is very small compared to the barrier energy of the 2^{nd}-nn jump (3.9 eV) thereby favoring the 6JC without ambiguity from an energy point of view.

Considering only atomic arrangements and the energy evolution during the successive jumps, it is difficult to conclude as to the occurrence of the global 6JC since no correlation data are available at the moment. Backward motion could easily occur in particular from step E since it seems more probable that the atom will go back to the more stable preceding position C (rather than G) that in addition requires a lower activation energy (D lower than F). Nevertheless, since all the activation energies of individual jumps are lower than 1.2 eV, all these successive jumps may be overcome and the 6JC thus achievable at high temperature.

In step G, we made the calculation for the jump of any possible 1^{st}-nn of the vacancy [Fig. 9(b)]. The cobalt atoms in the vertical plane containing the vacancy and the 2 Pt antisites have a slightly smaller barrier height than Pt1 (0.69 eV compared to 0.87 eV). But the total energy increases for the Co5 jump whereas it decreases for the Pt1 jump (+0.11 eV instead of −0.16 eV). The other cobalt atom jumps have a barrier similar to that of the Pt1 jump with the same energy balance as for Co5. The other Pt jumps have very high barriers. The Pt1 atom jump is so the most favorable from an energy point of view, which allows the 6-jump cycle to continue.

Another possible mechanism for interdiffusion without destroying the $L1_0$ long-range order is the migration of a double vacancy. This can be considered here because in thin films the surface is a close source of vacancies. Figure 10 shows the variation of the total energy as obtained by quenched molecular dynamics during the migration of a M -Pt-double vacancy for different mechanisms. In Fig. 10(a), a simultaneous jump of M and Pt is considered. During the M and Pt translation, the results are unchanged whether the M -Pt distance is kept constant or the Pt atom is left free to move. This mechanism includes 2 steps. After the first step, the atoms occupy antisite positions. After the second step, they occupy normal positions. The higher energy is obtained when both atoms are in a saddle position (1.72 eV higher than the initial energy).

If the jumps of M and Pt are successive, two mechanisms can be considered: either each atom crosses the bivacancy [Fig. 10(b): only single antisites are formed] or the atoms jump alternatively [Fig. 10(c): a nn pair of antisite is formed after the second step]. In the case of successive jumps [Fig. 10(b)], the maximum activation energy is 1.13 eV, but it

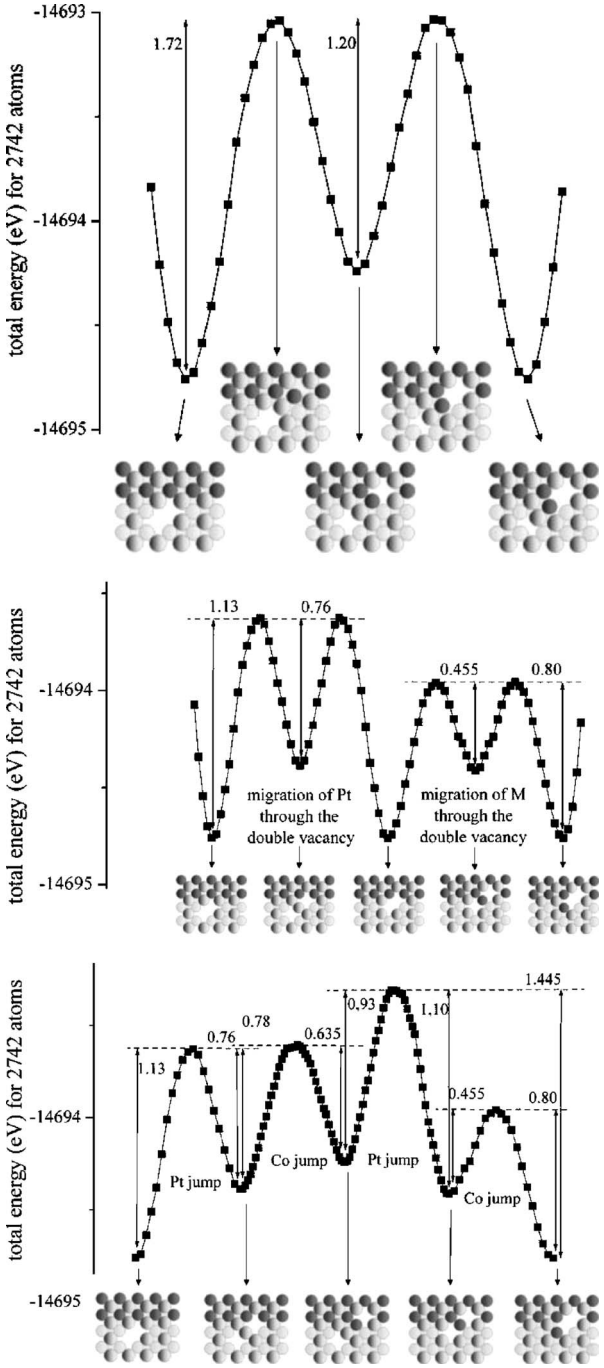

FIG. 10. Total energy variation for a bivacancy migration as calculated by quenched molecular dynamics and some configurations of the (100) plane containing the vacancies: (a) the Co-Pt pair is moving simultaneously, (b) the Co and Pt atoms cross the bivacancy successively, and (c) the Co and Pt atoms jump alternatively. The numbers give the energy differences in eV.

seems quite unlikely that the jumps of Pt and M occur in a concerted manner because in the middle state the Pt atom is far from the jumping M atom. In the case of alternate jumps [Fig. 10(c)], the maximal energy is found 1.445 eV higher than the initial value.

Thus, after examining the many possibilities for vacancy(ies) diffusion, we retained alternate jumps through a bivacancy and 6JC as the most favorable mechanisms from

energy considerations. The 2nd-nn jump mechanism is definitely ruled out by these simulations.

F. Formation energy of defects

From these simulations, we can also estimate the vacancy formation energy E_V by considering an average energy per (Pt, Co) couple of atoms: 2×5.36 eV (5.36 eV is the average energy per atom in CoPt obtained by TB-QMD in the perfect crystal) and by forming two distant (Pt, Co) vacancies to keep the composition constant. We obtain 1.38 eV per vacancy. No data exists on the energy of vacancy formation in the *M*Pt $L1_0$ phases. The order of magnitude can be obtained from the values in Ni (1.6 eV from Ref. 34 and 1.8 eV from Ref. 35) and Pt (1.5 eV from Ref. 34 and 1.4 eV from Ref. 35), which also crystallize in the fcc lattice. $E_V = 1.38$ eV is in good agreement with these orders of magnitude.

When forming only one vacancy, we obtain an energy increase of 2.03 eV for a Pt vacancy and 0.73 eV for a Co vacancy. The large value of the Pt vacancy formation energy is mainly due to the higher cost of the bond break, reflecting the fact that Pt has much stronger cohesion than Co. The relaxation contributions are only some tenths of eV.

The formation energy of a bivacancy (pair of nearest neighbor vacancies) is 2.36 eV. There is a small favorable energy balance due to the induced smaller number of broken bonds (0.4 eV and one *M*-Pt bond difference). This plays in favor of the bivacancy migration mechanisms.

Moreover, the formation of two antisites (exchanging a Co and a Pt at sufficient distance) costs 0.58 eV (0.29 eV per antisite). In comparison, during the 6JC, the formation of the first Pt antisite costs 0.21 eV whereas both the first Co antisite and the second Pt antisite cost 0.16 eV. The proximity of the vacancy thus slightly lowers the formation energy of the antisites.

G. Comparison with diffusion results

For the interdiffusion in the $(^{57}FePt/FePt)_N$ multilayers, Rennhofer *et al.*[27] have found an activation energy of 1.65 ± 0.29 eV along the *c* axis, much smaller than 3.17 ± 0.36 eV and 3.80 ± 0.45 eV, along the *a* and *c* axis, respectively, that were extracted from diffusion data measured by high-temperature radio tracer.[33] It should be noted that in bulk alloys the activation energy contains two terms, the vacancy formation and migration energies, of similar amplitude in most systems.

In thin films, the surface is a vacancy reservoir with a distance between 2 and 52 nm from any alloy atom. Thus the surface is quite near to the majority of the alloy atoms in comparison to the average distance between vacancies that can be evaluated in bulk samples from the vacancy formation energy E_V (between 1.4 and 1.8 eV, see Sec. V F) and entropy ΔS_V:

$$C_V \approx \exp(\Delta S_V/k_B - E_V/k_B T).$$

The vacancy formation entropy can be approximated by $\Delta S_V = -k_B c_V \ln(c_V)$, considering that the vacancies are randomly distributed on the lattice sites and using Stirling's formula.

We obtain an average distance between vacancies within the interval 97 nm ($E_V = 1.4$ eV) to 540 nm ($E_V = 1.8$ eV) at 900 K, to be compared with the 50 nm thickness of the films (same thickness in Ref. 27). The formation of vacancies is thus no longer a limiting process. The vacancy formation energy does not have to be considered in those thin films at this temperature and the apparent activation energy can be restricted to the migration energy that we have calculated by TB-QMD. This explains why the activation energy measured by Rennhofer *et al.*[27] is half that measured in bulk alloys: they measured the vacancy-migration energy alone. The difference 2.15 ± 0.74 eV is in good agreement with the expected vacancy-formation energy.

The experimental value of Ref. 27 (1.65 ± 0.29 eV) is in qualitative agreement with the correlated simultaneous (1.72 eV) or alternate (1.445 eV) jumps through a bivacancy and the correlated 6JC mechanism (1.40 eV). At this stage it is not possible to go further in the argumentation on the occurrence of the different mechanisms, as a function of temperature for instance. In order to evaluate global activation energy together with their corresponding attempt frequency, molecular dynamics simulations at elevated temperature[36] have to be performed.

VI. CONCLUSION

$L1_0$ ordered $FeNiPt_2$ alloy thin films have been obtained by 900 K *ex situ* annealing of NiPt/FePt/MgO(001) fabricated by molecular beam epitaxy. They present a high chemical order and a perpendicular magnetic anisotropy. MFM images display highly interconnected stripes corresponding to up and down orientations of the magnetization, in agreement with the anisotropy deduced from the hysteresis loops. Relative to FePt, $FeNiPt_2$ films exhibit a decrease in the coercivity and the Curie temperature, which makes $FeNiPt_2$ more suitable than FePt for high-density magnetic recording using the current industry technology, in spite of the decrease in the saturation and remanent magnetizations. Moreover, the interdiffusion at 900 K takes place without destroying the $L1_0$ long-range order, whereas at 800 K $L1_0$ long-range order increases in both layers without any interdifffusion. Quenched molecular dynamic simulations have been used to estimate the activation energy of different mechanisms able to yield Fe and Ni migration along the *z* axis of the $L1_0$ phase while conserving the $L1_0$ long-range order. The simulation results clearly show that the correlated 6-jump cycle and bivacancy migration mechanisms are favored energetically compared to the 2nd-nn jump mechanism. The activation energies found for these mechanisms are in good agreement with the experimental values found by Rennhofer *et al.*[27] Molecular dynamics simulations at elevated temperature[36] are in progress to determine which mechanism is actually found and with what attempt frequency.

ACKNOWLEDGMENTS

We are indebted to Mirek Kozlowski for writing the batch files in perl to make the TB-QMD calculations and to Marie-Claire Cadeville, Pierre Panissod, and Martin Bowen for critical reading of the paper.

*Email address: vero@ipcms.u-strasbg.fr

[1] G. H. O. Daalderop, P. J. Kelly, and M. F. H. Schuurmans, Phys. Rev. B **44**, R12054 (1991).
[2] A. Cebollada, D. Weller, J. Sticht, G. R. Harp, R. F. C. Farrow, R. F. Marks, R. Savoy, and J. C. Scott, Phys. Rev. B **50**, 3419 (1994).
[3] M. Abes, O. Ersen, D. Muller, M. Acosta, C. Ulhaq-Bouillet, A. Dinia, and V. Pierron-Bohnes, Mater. Sci. Eng., C **23**, 229 (2003).
[4] O. Ersen, V. Parasote, V. Pierron-Bohnes, M. C. Cadeville, and C. Ulhaq-Bouillet, J. Appl. Phys. **93**, 2987 (2003).
[5] R. F. C. Farrow, D. Weller, R. F. Marks, M. F. Toney, A. Cebollada, and G. R. Harp, J. Appl. Phys. **79**, 5967 (1996).
[6] M. H. Hong, K. Hono, and M. Watanabe, J. Appl. Phys. **84**, 4403 (1998).
[7] R. A. Ristau, K. Barmak, L. H. Lewis, K. R. Coffey, and J. K. Howard, J. Appl. Phys. **86**, 4527 (1999); V. Parasote, M. C. Cadeville, G. Garreau, and E. Beaurepaire, J. Magn. Magn. Mater. **198**, 375 (1999).
[8] T. Thomson, M. F. Toney, S. Raoux, S. L. Lee, S. Sun, C. B. Murray and B. D. Terris, J. Appl. Phys. **96**, 1197 (2004).
[9] H. Kanazawa and T. Suzuki, J. Appl. Phys. **91**, 7538 (2002).
[10] C. E. Dahmani, M. C. Cadeville, J. M. Sanchez, and J. L. Moran-Lopez, Phys. Rev. Lett. **55**, 1208 (1985); C. E. Dahmani, Ph.D. thesis, Louis Pasteur University, Strasbourg, France (1985).
[11] S. Shimizu and E. Hashimoto, J. Jpn. Inst. Met. **35**, 902 (1971).
[12] G. T. Stevens, M. Hatherly, J. S. Bowles, J. Mater. Sci. **13**, 499 (1978).
[13] A. Cebollada, R. F. C. Farrow, and M. F. Toney, *Magnetic Nanostructures* (American Scientific Publishers, 2002), p. 93.
[14] H. E. Fischer, H. Fischer, O. Durand, O. Pellegrino, S. Andrieu, M. Piecuch, S. Lefèbvre, and M. Bessière, Nucl. Instrum. Methods Phys. Res. B **97**, 402 (1995).
[15] In the whole paper, except when explicitly specified, the indices of the planes and Bragg peaks will be given using the indices of the substrate.
[16] Due to the tetragonalization of the lattice associated to the $L1_0$ ordering, the fundamental peaks of the different variants are split.
[17] L. H. Schwartz and J. B. Cohen, J. Appl. Phys. **36**, 598 (1965).
[18] J. A. Ibers and W. C. Hamilton, *International Tables for X-ray Crystallography* (The Kynoch Press, Birmingham, 1974), Vol. 4.
[19] P. Villars and L. D. Calvert, *Pearson's Handbook of Crystallographic Data for Intermetallic Phases* (American Society for Metals, Metals Park, OH, 1985), Vol. 3.
[20] G. Armelles, D. Weller, B. Rellinghaus, P. Caro, A. Cebollada, and F. Briones, J. Appl. Phys. **82**, 4449 (1997).
[21] V. Gehanno, A. Marty, B. Gilles, and Y. Samson, Phys. Rev. B **55**, 12552 (1997).
[22] D. Halley, P. Auric, P. Bayle-Guillemaud, B. Gilles, A. Marty, and D. Jalabert, J. Appl. Phys. **91**, 9757 (2002).
[23] Y. Gauthier, Surf. Rev. Lett. **3**, 1663 (1996); Y. Gauthier, P. Dolle, R. Baudoing-Savois, W. Hebenstreit, E. Platzgummer, M. Schmid, and P. Varga, Surf. Sci. **396**, 137 (1998).
[24] N. Li, B. M. Lairson, and O. H. Kwon, J. Magn. Magn. Mater. **205**, 1 (1999).
[25] C. Kooy and U. Enz, Philips Res. Rep. **15**, 7 (1960).
[26] S. Okamoto, N. Kikuchi, O. Kitakami, T. Miyazaki, Y. Shimada, and K. Fukamichi, Phys. Rev. B **66**, 024413 (2002).
[27] M. Rennhofer, B. Sepiol, M. Sladecek, S. Stankov, G. Vogl, R. Kozubski, M. Kozlowski, R. Rüffer, and J. Meersschaut, Phys. Rev. B (to be published).
[28] S. Divinski, Chr. Herzig, Intermetallics **8**, 1357 (2000).
[29] M. Rennhofer, B. Sepiol, W. Löser, and G. Vogl, Intermetallics **11**, 573 (2003).
[30] C. Goyhenex, H. Bulou, J. P. Deville, and G. Treglia, Phys. Rev. B **60**, 2781 (1999).
[31] C. Mottet, G. Tréglia, and B. Legrand, Phys. Rev. B **46**, 16018 (1992).
[32] F. Hontifide, R. Ferrando, and A. C. Levi, Surf. Sci. **366**, 306 (1996).
[33] A. Kushida, K. Tanaka, and H. Numakura, Mater. Trans. **44**, 59 (2003).
[34] S. M. Foiles, M. I. Baskes, and M. S. Daw, Phys. Rev. B **33**, 7983 (1986).
[35] T. Korhonen, M. J. Puska, and R. M. Nieminen, Phys. Rev. B **51**, 9526 (1995).
[36] C. Goyhenex, Surf. Sci. **600**, 15 (2006).